BIOPHYSICS

Light-induced protein structural dynamics in bacteriophytochrome revealed by time-resolved x-ray solution scattering

Sang Jin Lee[1,2]†, Tae Wu Kim[3]†, Jong Goo Kim[1,2], Cheolhee Yang[1,2], So Ri Yun[1,2], Changin Kim[1,2], Zhong Ren[4], Indika Kumarapperuma[4], Jane Kuk[5], Keith Moffat[5], Xiaojing Yang[4,6]*, Hyotcherl Ihee[1,2]*

Bacteriophytochromes (BphPs) are photoreceptors that regulate a wide range of biological mechanisms via red light–absorbing (Pr)–to–far-red light–absorbing (Pfr) reversible photoconversion. The structural dynamics underlying Pfr-to-Pr photoconversion in a liquid solution phase are not well understood. We used time-resolved x-ray solution scattering (TRXSS) to capture light-induced structural transitions in the bathy BphP photosensory module of *Pseudomonas aeruginosa*. Kinetic analysis of the TRXSS data identifies three distinct structural species, which are attributed to lumi-F, meta-F, and Pr, connected by time constants of 95 μs and 21 ms. Structural analysis based on molecular dynamics simulations shows that the light activation of PaBphP accompanies quaternary structural rearrangements from an "II"-framed close form of the Pfr state to an "O"-framed open form of the Pr state in terms of the helical backbones. This study provides mechanistic insights into how modular signaling proteins such as BphPs transmit structural signals over long distances and regulate their downstream biological responses.

INTRODUCTION

Light is one of the most important environmental stimuli in living organisms. At the molecular level, photoreceptors detect light signals and convert them into biological signals, allowing organisms to respond and adapt to changes in their light environment. The phytochrome superfamily acts as photoreceptors with biliverdin as their chromophores. In plants, bacteria, and fungi, they mediate a wide range of light responses, such as seed germination, floral induction, phototaxis, and photo-acclimation (*1*–*5*). Naturally occurring phytochromes are large, modular, and dimeric signaling proteins. Classical phytochromes, including bacteriophytochromes (BphPs), consist of a photosensor module containing Per-Arnt-Sim (PAS), cGMP phosphodiesterase- adenylate cyclase-FhlA (GAF), and phytochrome-related (PHY) domains, followed by a C-terminal output moiety (Fig. 1A). Together, the PAS, GAF, and PHY domains form a fully photoactive photosensory module in which the biliverdin chromophore is embedded in the GAF domain via a covalent linkage to a cysteine residue (*6*–*12*). Upon photoisomerization of the biliverdin chromophore at the C15═C16 double bond between the C and D pyrrole rings, phytochromes undergo reversible photoconversion between the far-red –absorbing (Pfr) and red –absorbing (Pr) states, which display distinct structural and spectral properties (Fig. 1A) (*4*, *13*–*16*). In BphPs, the output histidine kinase (HK) domain, which is connected to the C terminus of the photosensory module via a long signaling helix, undergoes light-dependent autophosphorylation. Members of the BphP superfamily are categorized as either canonical or bathy types, based on their photoconversion behavior. Canonical BphPs adopt the parental Pr state in the dark and convert it into the Pfr state upon illumination with red light. In contrast, bathy BphPs adopt the parental Pfr state in the dark and convert it into the Pr state upon illumination with far-red light (fig. S1) (*10*, *17*, *18*).

Extensive studies have been conducted to investigate the photoactivation mechanisms by which BphPs undergo photoisomerization and trigger downstream responses. In a general reaction scheme, the absorption of light triggers photoisomerization that is associated with the rotation of the C15═C16 double bond at a picosecond time scale (Fig. 1A) (*4*, *13*). Photoisomerization is followed by slower steps involving several spectrally distinct intermediate states before the formation of the final photoproducts, either the Pfr or Pr states, at a micro- to millisecond time scale. Ultrafast studies also revealed that relaxation of the chromophore-binding pocket is tightly coupled to chromophore photoisomerization during the formation of early photoproducts at a time scale ranging from tens to hundreds of picoseconds (*14*, *15*, *19*, *20*). Nevertheless, these spectroscopic studies directly probe the electronic structure of the chromophore but do not detect global structural changes in the protein moiety. Thus, it remains unclear how these local, light-induced structural changes are transmitted beyond the chromophore-binding pocket to the remote C-terminal HK output domain. Although the crystal structures of dark-adapted Pfr and Pr states have been determined for several BphPs (*6*–*9*, *21*, *22*), it has proven difficult to crystallize BphPs in their light-activated forms. DrBphP, a canonical BphP from *Deinococcus radiodurans*, is the only BphP with crystal structures in both dark-adapted Pr and light-activated Pfr states (*8*, *23*). Important questions regarding the signaling dynamics of BphPs remain unanswered. Specifically, we ask the following questions: In what order and at what time scale do these structural events occur in the liquid solution phase? When compared with canonical BphPs, do bathy BphPs undergo similar structural changes during their transition from dark-adapted Pfr to light-activated Pr states?

[1]Department of Chemistry and KI for the BioCentury, Korea Advanced Institute of Science and Technology (KAIST), Daejeon 34141, Republic of Korea. [2]Center for Advanced Reaction Dynamics, Institute for Basic Science (IBS), Daejeon 34141, Republic of Korea. [3]Department of Chemistry, Mokpo National University, Muan-gun, Jeollanam-do, 58554, Republic of Korea. [4]Department of Chemistry, University of Illinois at Chicago, Chicago, IL 60607, USA. [5]Department of Biochemistry and Molecular Biology, The University of Chicago, Chicago, IL 60637, USA. [6]Department of Ophthalmology and Vision Sciences, University of Illinois at Chicago, Chicago, IL 60607, USA.
*Corresponding author. Email: xiaojing@uic.edu (X.Y.); hyotcherl.ihee@kaist.ac.kr (H.I.)
†These authors contributed equally to this work.

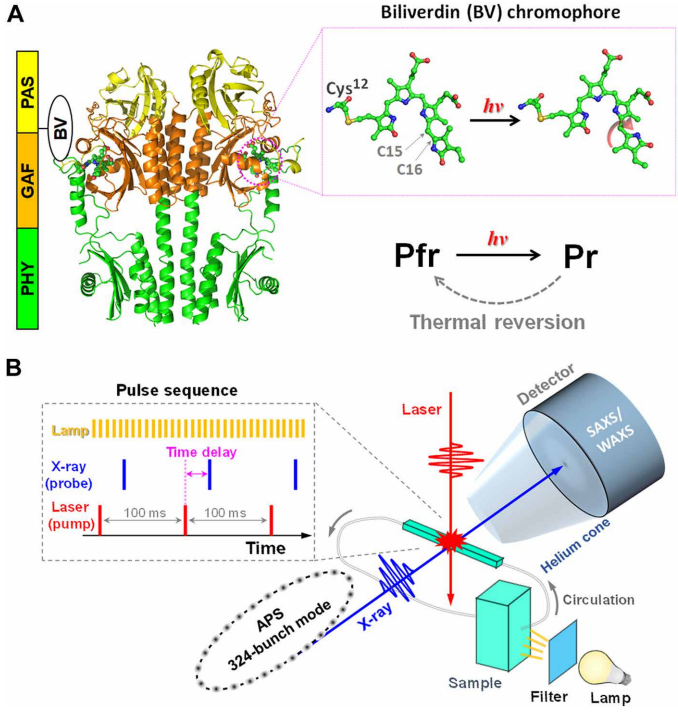

Fig. 1. Protein structure and photocycle of bathy PaBphP and the experimental scheme for time-resolved x-ray solution scattering. (**A**) Three-dimensional structures of the photosensory module of PaBphP and its biliverdin chromophore. The photosensory module consists of the PAS, GAF, and PHY domains. The inset shows the molecular structure of the biliverdin chromophore (ball-and-stick), which is covalently bound to the PAS domain through a cysteine residue (Cys^{12}). Upon far-red light activation, the photoreaction is initiated toward the formation of the Pr state, accompanying the structural changes in the biliverdin chromophore. (**B**) Conceptual scheme of time-resolved x-ray solution scattering (TRXSS). Picosecond laser pulses (pump) with the wavelength of 780 nm are used to excite protein molecules and, subsequently, with a well-defined time delay, x-ray pulses (probe) with the energy of 12 keV are delivered to observe the laser-induced structural changes recorded in both small-angle/wide-angle x-ray scattering (SAXS/WAXS) patterns. The inset shows the temporal sequences of three different beams including the pump and probe pulses. APS, Advanced Photon Source.

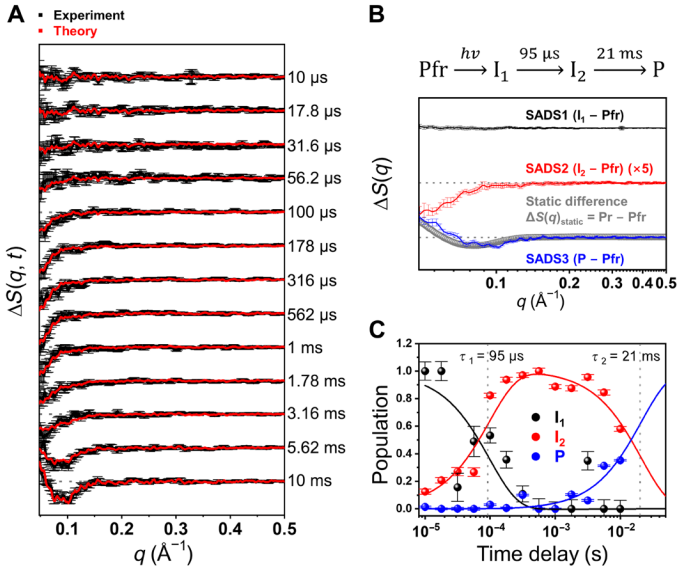

Fig. 2. Global kinetic analysis of the TRXSS data. (**A**) Experimental (black) and theoretical (red) difference scattering curves. (**B**) Proposed kinetic model and species-associated difference scattering curves (SADSs). The top scheme shows the proposed kinetic model for the far-red–induced transition of PaBphP. The bottom panel displays the SADSs determined from the PCA analysis. SADS1 (black) and SADS2 (red) correspond to I_1 and I_2 states in the kinetic model, respectively. SADS3 (blue) corresponds to the final photoproduct labeled as P and is compared to the static difference curve (gray dots), $\Delta S_{static}(q)$. (**C**) Time-dependent populations of the transient species.

RESULTS

Time-resolved x-ray solution scattering

To address these questions, we apply time-resolved x-ray solution scattering (TRXSS) to capture the photoinduced structural dynamics in PaBphP, a bathy BphP from *Pseudomonas aeruginosa*. The difference scattering method enabled by TRXSS, also known as time-resolved x-ray liquidography (*24*–*39*), is highly sensitive to global structural changes in solution arising from an experimental trigger. Kinetic analysis of light-induced difference scattering profiles from PaBphP identifies three distinct structural species on the micro- to millisecond time scale in the photoconversion pathway from the parental dark-adapted Pfr state to the light-activated Pr state. A combination of kinetic analysis of the TRXSS data with structural analysis aided by molecular dynamics (MD) simulations (*40*, *41*) establishes the reaction mechanism and tracks the protein structural changes in PaBphP. Our structural analysis shows that PaBphP undergoes an extensive conformational change from an "II"-framed structure of the Pfr state to an "O"-framed structure of the Pr state in terms of its helical backbones. This demonstrates that the structural changes involved in the photoinduced transition of PaBphP are distinct from those of canonical BphPs (*8*, *23*, *42*).

To probe the dynamics of the Pfr-to-Pr photoconversion pathway, we collected TRXSS data in two time series, which, when combined, span four decades from 10 μs to 10 ms (fig. S2A). As the linear absorption spectra of the Pr and Pfr states overlap substantially in the red region (fig. S3D), a dynamic equilibrium is reached at room temperature between these two distinct states: Their composition ratio depends on the relative amount of red and far-red light in an ambient light environment. To preferentially excite the Pfr state, a 780-nm laser was used in laser pump–x-ray probe experiments. A flow cell delivered protein (25 to 30 mg/ml) to the sample capillary at a linear flow rate of 10 mm/s. The sample reservoir was kept in ice under constant illumination with red light to minimize the accumulation of Pr in the reference state. To ensure accurate light-induced difference measurements, a reference scattering pattern was collected for each decade in time at a negative time delay (−5 or −10 μs) before excitation at 780 nm (Materials and Methods and Fig. 1B).

In the light-induced difference scattering curves, we observed a significant decrease in scattering intensity in the small-angle region ($q < 0.2$ Å^{-1}) over tens to hundreds of microseconds (Fig. 2). In the millisecond range, more difference features appear in the small-angle region and only small differences with marginal significance in the wide-angle region (0.3 Å$^{-1} < q < 1.0$ Å^{-1}). To characterize the kinetic behaviors of the light-induced protein, the merged difference scattering curves, $\Delta S(q, t)$, over the entire time range were obtained by scaling data from the two different time series (Materials and Methods and figs. S2 and S4). Global kinetic analysis using singular value decomposition (SVD) and principal components analysis

(PCA) is described in Materials and Methods. Fitting the corresponding right singular vectors (RSVs) with the sum of exponential functions sharing common time constants yielded two different time constants, 95 (± 25) μs and 21 (± 32) ms (Fig. 2). The uncertainty associated with the second time constant was large, owing to the limited time range (up to 10 ms) of the experimental data when compared with the corresponding time scale (21 ms).

In the subsequent kinetic analysis using PCA, we used a sequential kinetic model involving three transient species with time constants of 95 μs and 21 ms, which were obtained from the RSVs, and extracted three species-associated difference scattering curves (SADSs), which contain direct information on the structural changes associated with the formation or decay of the transient species (Fig. 2B). In this kinetic model, the first species, I_1, formed within the experimental time resolution, is converted to the second species, I_2, with a time constant of 95 μs. Subsequently, I_2 is converted to the third species, P, with a time constant of 21 ms (Fig. 2C). The theoretical time-resolved difference scattering curve at each time delay is generated by the sum of the SADSs, obeying the sequential kinetics shown in Fig. 2B. The final theoretical difference scattering curves show excellent agreement with the experimental curves, confirming that the sequential kinetic model satisfactorily describes the experimental data (Fig. 2A). The first SADS (SADS1), which corresponds to I_1, has nearly flat features over the entire q range, although some fine features can be observed when magnified. Such a small difference signal for I_1 indicates that the formation of I_1 does not involve detectable protein structural changes within the current signal-to-noise ratio (SNR). In contrast, SADS2, which corresponds to I_2, shows relatively small monotonous features in the q region at <0.2 $Å^{-1}$, suggesting that the second species is structurally distinct from the parental Pfr and I_1 state. SADS3, which corresponds to P, is characterized by a prominent negative peak with a significant amplitude at q of approximately 0.09 $Å^{-1}$. The predominant scattering intensities of SADS2 and SADS3 in the small-angle region (q < 0.3 $Å^{-1}$) support that PaBphP undergoes global light-induced structural arrangements. SADS3 has a significantly larger intensity than SADS2, indicating that P involves relatively larger structural changes than I_2, and major structural changes occur in the I_2-to-P transition. The time-dependent population of SADSs shows that the population of P increases as that of I_2 decreases at a time scale of tens of milliseconds (Fig. 2C).

Light-induced structural changes

To investigate the structural changes during the photoinduced transition of PaBphP, a structural analysis guided by MD simulations on the observed SADSs was conducted. In principle, each SADS contains information about the protein structure of the corresponding intermediate species. As the scattering feature of SADS1 was found to be insignificant within the experimental resolution, structural analysis of the TRXSS data was performed on SADS2 and SADS3. First, nonequilibrium MD (NEMD) simulations were used to generate candidate structures that account for the scattering patterns of SADS2 and SADS3. In NEMD, the structure of the Pfr state in PaBphP was used as a starting point, and then various protein structures with target shapes were generated from the starting Pfr structure. The targeted shapes of the protein structures accessed in the NEMD were established by considering the various conformations of BphPs reported in the crystallographic studies (*7*–*9*, *23*). Specifically, the crystal structures of the Pfr and Pr states in BphPs can be categorized into three representative conformational frames in terms of the geometry of their helical backbones: (i) II-frame, (ii) O-frame, and (iii) Y-frame (fig. S1C). For instance, the reported crystal structures of dark-adapted Pfr, dark-adapted Pr, and light-Pfr represent the II-, O-, and Y-frames, respectively. In the structural analysis, we first assumed that the Pfr, I_2, and P states could adopt one of the three frames and then performed a structural analysis against SADS2 and SADS3. As both Pfr and I_2 (or P) have three possibilities (II-, O-, and Y-frames), nine combinations are possible (Fig. 3, A and D). On the basis of these nine different combinations, various candidate structures were generated from the NEMD simulations using the pulling approach within a feasible simulation time. For these simulations, two pulling axes between the two helical backbones were defined as plausible reaction coordinates to generate an O-framed structure, and one pulling axis between the two helical backbones was defined as a plausible reaction coordinate to generate a Y-framed structure. The sampled candidate structures used in the structural analysis are shown in fig. S5. The theoretical x-ray static scattering curves corresponding to the individual protein conformations were calculated from the MD-sampled structures, and the theoretical "difference" scattering curves were generated by subtracting the theoretical static scattering curves for Pfr from those of I_2 (or P). Then, the theoretical difference curves were fitted to the experimental curves of SADS2 and SADS3 by minimizing the χ^2 values between the theoretical and experimental curves, which quantified the discrepancy between the theoretical and experimental data (see Materials and Methods and Eq. 2 for details).

The residuals between the best-fit curve and SADS2 (SADS3) with the corresponding χ^2 values for all nine combinations of I_2 (P) and Pfr structures are shown in Fig. 3 (A and D). In the structural analysis of SADS2, the optimal model with the smallest residual and χ^2 value was obtained when both Pfr and I_2 had II-framed structures (Fig. 3A). In this case, the optimal theoretical curve showed excellent agreement with that of SADS2 (Fig. 3B). From the optimal model, the representative protein structures for Pfr and I_2 were extracted, as depicted in Fig. 3C, and compared with each other for the structural details about the transition from Pfr to I_2 (via I_1). To describe the structural motions of the optimal structures in a quantitative manner, we measured the distance between two Arg^{321} residues (termed as Q1) and the distance between two Ala^{332} residues (termed as Q2) as major structural coordinates, as the Arg^{321} and Ala^{332} residues are located near the middle and at the C termini of the helical backbones, respectively. A comparison of the optimal protein structures shows that Pfr has Q1 and Q2 of 1.44 and 1.86 nm, and those distances are changed to 1.52 and 1.90 nm in I_2, respectively (Fig. 3C). This marginal change in the major structural coordinates demonstrates that the transition from Pfr to I_2 (via I_1) accompanies a slight opening of the II-framed structure in terms of the helical backbones (Fig. 3C).

In contrast, the structural analysis of SADS3 showed that the optimal model with the smallest residual and χ^2 value was obtained when Pfr had an II-framed structure and P had an O-framed structure (Fig. 3, D and E). In the O-framed structure, Q1 and Q2 are 5.18 and 3.18 nm, respectively, which are much larger than those in I_2 (Fig. 3F). We note that in the transition from I_2 to P, the change in Q1 with 3.66 nm is much larger than that of Q2 with 1.28 nm, causing the helical backbones of P to bend. Although there are no physical constraints applied to the structure of the Pfr state in the structural analysis of SADS2 and SADS3, the Pfr structure obtained from the analysis of SADS2 shows an almost identical conformation

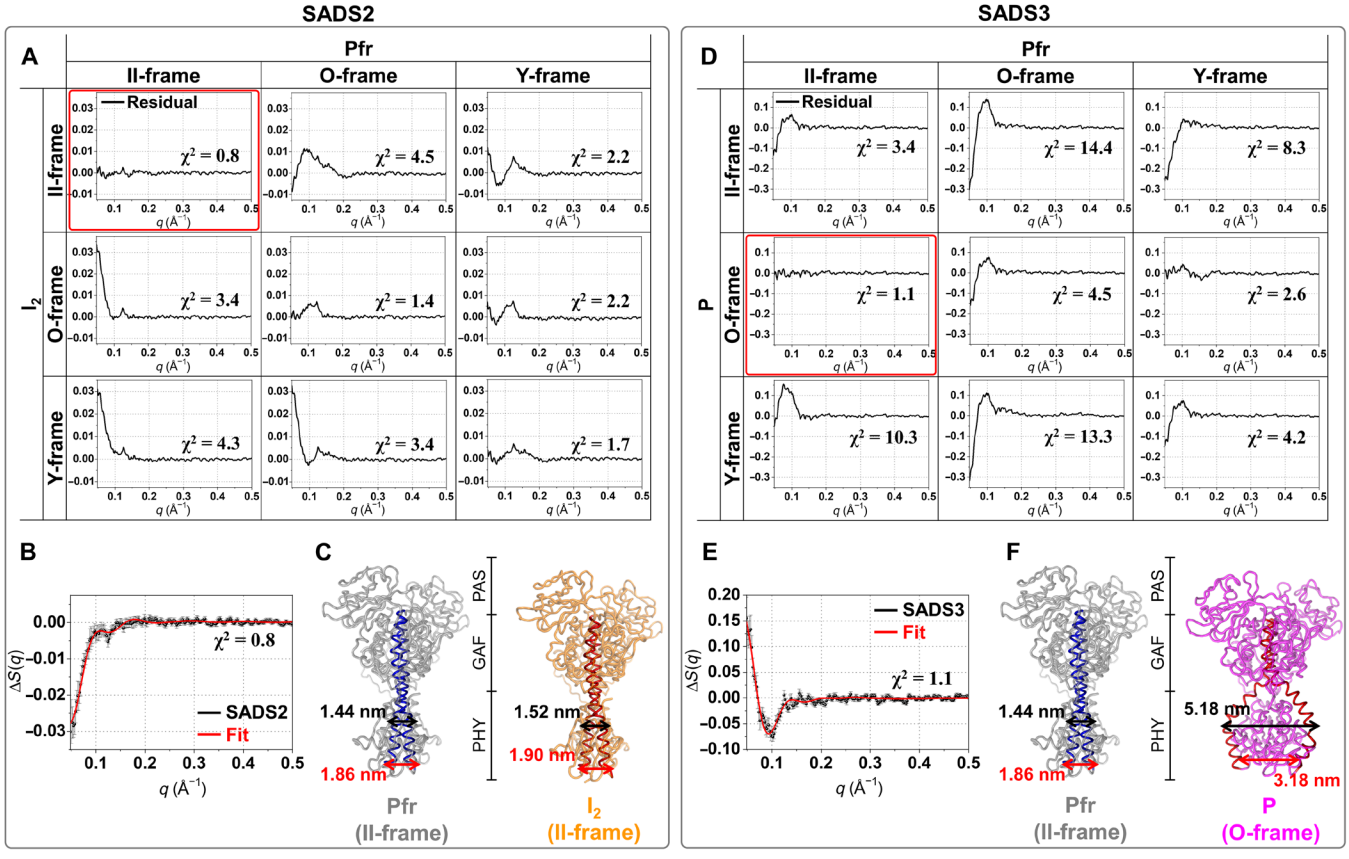

Fig. 3. Structural analysis of the TRXSS data. (**A**) Each panel shows the residual (black lines) and the χ^2 value between SADS2 and the best-fit theoretical scattering curve determined from the structural analysis, in which the structures of I_2 and Pfr are assumed to have one of the three different conformations (II-, O-, and Y-frame). The best fit with the smallest residual and smallest χ^2 value was obtained when both Pfr and I_2 have II-framed structures (indicated by a red box). (**B**) Comparison of SADS2 (black dot) and the theoretical scattering curve (red line) that gives the best agreement with SADS2. (**C**) Representative protein conformations for Pfr (gray ribbon) and I_2 (green ribbon) from the optimal structural model. (**D**) Each panel shows the residual (black lines) and the χ^2 value between SADS3 and the best-fit theoretical scattering curve determined from the structural analysis, in which the structures of P and Pfr were assumed to be one of the three different conformations (II-, O-, and Y-frame). The best fit with the smallest residual and smallest χ^2 value was obtained when Pfr has II-framed structure and P has O-framed structure (indicated by a red box). (**E**) Comparison of SADS3 (black dot) and the theoretical scattering curve (red line) that gives the best agreement with SADS3. (**F**) Representative protein conformations for P (gray ribbon) and Pfr (magenta ribbon) from the optimal structural model. The Pfr structures for SADS2 and SADS3, determined from the structural analysis, show almost identical protein conformations with a root mean square deviation of 0.081 nm between them. For clarity, in (C) and (F), the helical backbones in I_2 (or P) and the Pfr are color-coded by the red and blue ribbons, respectively. The distances between Arg^{321} residues and between Ala^{332} residues are indicated by the black and red arrows, respectively.

with that from SADS3 within a root mean square deviation value of 0.081 nm between them. The results of the structural analysis suggest that bathy PaBphP undergoes a large conformational change from the initial II-framed structure in Pfr to the final O-framed structure in P via the opened II-framed structure in I_2.

DISCUSSION

The combined kinetic and structural analyses of the TRXSS data show that the following kinetic model is consistent with the light activation of Pfr to Pr in PaBphP

$$\mathrm{Pfr} \xrightarrow{\mathrm{hv}} \mathrm{I_1} \xrightarrow{95\ \mu s} \mathrm{I_2} \xrightarrow{21\ ms} \mathrm{P}$$

where Pfr is the initial state, I_1 is the first intermediate, I_2 is the second intermediate, and P is the final photoproduct. During the photoinduced transition, I_2 is formed from I_1 with a time constant of 95 μs and converts into P with a time constant of 21 ms. The time constants determined from spectroscopic studies are listed and compared with those from this work in Table 1. According to a study using femtosecond-resolved fluorescence and absorption spectroscopy, the primary event of PaBphP associated with the photoisomerization of the biliverdin chromophore occurs in the picosecond time range, which is shorter than the temporal resolution of this study and therefore not observable (*14*). A recent x-ray crystallographic study of DrBphP reported that the twisting of tetrapyrrole rings occurs in the early picosecond time range (*43*). As SADS1 has a flat signal, the conformational changes during the formation of I_1 can be solely attributed to local structural changes around the biliverdin chromophore and its surrounding residues, which were not detectable in our experiment. In longer time scales, the TRXSS captured the time constants of 95 μs and 21 ms. According to a previous study using transient absorption (TA) spectroscopy (*44*), the time constants of 230 μs and 15.9 ms were identified as lumi-F → meta-F and meta-F → Pr transitions, respectively. Considering that the time constants (95 μs and 21 ms) observed using TRXSS are comparable

Table 1. Comparison of time constants determined from previous spectroscopic studies of PaBphP and those from the current work.

	Fs-resolved fluorescence and absorption*	Laser flash–induced time-resolved absorption†	This work‡
Photoisomerization	1 ps, 4 ps		
Pfr → lumi-F		6 μs	
lumi-F → meta-F		230 μs	95 μs
meta-F → Pr		15.9 ms	21 ms

*Femtosecond (Fs)–resolved fluorescence and absorption method (*14*). †Laser flash–induced time-resolved absorption spectroscopy (*44*). ‡Time-resolved x-ray solution scattering.

to those (230 μs and 15.9 ms) observed using TA spectroscopy, the species of I_1, I_2, and P in the kinetic model can be assigned as lumi-F, meta-F, and Pr states, respectively. We note that the spectral change with 230 μs from the TA study was rather obscure, whereas the last process with 15.9 ms showed a clear spectral feature linked to the formation of the photoproduct Pr state. This is consistent with the TRXSS data, which show that the scattering signal changes for 95 μs and 21 ms are weak and strong, respectively. We also conducted a static x-ray scattering experiment for the dark-incubated state, dominated by the Pfr state, and the illuminated state, dominated by the Pr state. The difference in the static scattering curves, ΔS_{static}(Pr − Pfr), shows good agreement with the scaled SADS3, ΔS(P − Pfr) (Fig. 2B, fig. S3, and the Supplementary Materials), further supporting that P corresponds to Pr.

The detailed structural dynamics of bathy BphPs, starting from the parental Pfr state toward the photoproduct Pr state, were not previously reported: They were instead assumed on the basis of those of other canonical BphPs such as DrBphPs or cyanobacterial phytochromes, which have parental Pr states (*8*, *42*, *45*, *46*). Here, structural analysis of the TRXSS data has provided comprehensive information on the conformational changes in the photoinduced conversion process from Pfr to Pr, as summarized in Fig. 4. The structure of I_1, corresponding to lumi-F, was not determined by structural analysis. Considering the flat feature of SADS1, we have tentatively suggested that I_1 has the same structure as Pfr, so far as TRXSS might discern different structures within the SNR. Thus, I_1 is likely to adopt II-framed geometry, like that of Pfr. According to the structural analysis, I_2, corresponding to meta-F, has a protein conformation similar to that in the Pfr state that was previously reported from crystallographic studies (*6*, *7*, *47*), but the distances (Q1 and Q2) between the two long straight helical backbones juxtaposed at the dimer interface are slightly increased by 0.08 and 0.04 nm, respectively, relative to those in the Pfr state. The transition from I_2 to P (Pr) accompanies the formation of an O-framed geometry in the helical backbone (Fig. 4). The transition from the II-framed geometry in Pfr to the O-framed geometry in Pr is consistent with the size exclusion chromatography results, which showed that PaBphP has a larger effective hydrodynamic radius in the illuminated state when compared to the dark-incubated state (see the Supplementary Materials and fig. S3 for details). A crystallographic study reported that far-red irradiation of bathy Agp2 crystals induced the loss of the diffraction pattern (*22*). Considering our observations, it can be inferred that in bathy Agp2, a large conformational change, similar to that in PaBphP, can occur in the crystals, and ultimately result in the loss of a well-ordered crystal structure. Meanwhile, according to

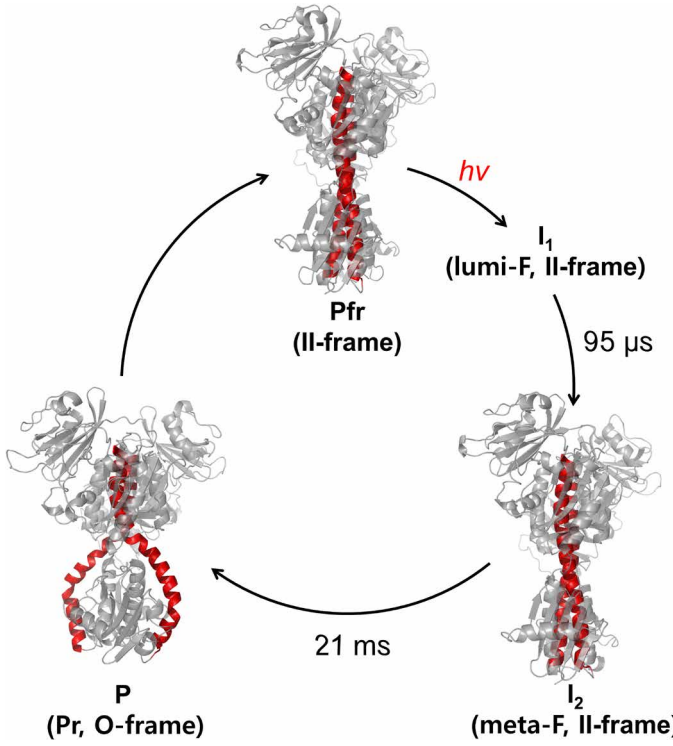

Fig. 4. Structural dynamics of the PaBphP photocycle revealed using TRXSS. The photocycle of PaBphP includes three intermediates (I_1, I_2, and P) and two time constants (95 μs and 21 ms), as determined from the kinetic analysis of the scattering data. The optimal protein conformations of the parent state (Pfr) and the two intermediates (I_2 and P) were extracted from the structural analysis based on the NEMD. On the basis of the results from the spectroscopic study (*44*) and the static scattering experiment, I_1, I_2, and P can be assigned as lumi-F, meta-F, and Pr states, respectively. The optimal protein structures show that Pfr and I_2 adopt the II-framed geometries in terms of helical backbones. The nearly parallel backbones in I_2 become fully open with the O-framed geometry in the photoproduct P state. For clarity, the helical backbones in the optimal structures are color-coded in red, and the other structures are color-coded in gray.

studies of canonical DrBphP (*8*), which is the only case in which the protein structures of both Pfr and Pr states were reported, the parental Pr state adopts the O-framed geometry, which is quite similar to that observed in the P state of PaBphP. In contrast, the photoproduct Pfr state of DrBphP has a Y-framed geometry, which differs from the nearly parallel II-frame in the Pfr state of PaBphP. It is noted that in our structural analysis, we also considered the

possibility that the parental Pfr state of PaBphP adopts the Y-framed geometry in addition to II-framed geometry. Such a case failed to reproduce the experimental data in the small-angle x-ray scattering (SAXS) region of SADS2 and SADS3 (Fig. 3, A and D). These results indicate that the light-induced structural dynamics in bathy PaBphPs are significantly different from those in canonical BphPs.

Meanwhile, crystallographic studies of bathy Agp2 and canonical DrBphP suggested the possibility of a local structural change from α helices to β sheets in the vicinity of the PHY arms (*8*, *22*, *45*). In the NEMD simulation to sample the candidate structures, the α helix–to–β sheet transition in the PHY arm was not enforced, and thus this local structure could not be properly described in the optimal structures of I_2 and P. To check whether the TRXSS data could provide any experimental evidence for the local structural transition around the PHY arm, we performed an additional analysis by intentionally considering β sheet formation in I_2 and Pr (see the Supplementary Materials and fig. S6). The theoretical difference scattering curves obtained from the structural analysis with the deliberate formation of the β sheet around the PHY arm show good agreement with the experimental data, but the degree of agreement is comparable to the case of the theoretical curves from the analysis without considering β sheet formation (fig. S6). These results suggest that these subtle structural changes around the PHY arm are not detectable within the current SNR of the scattering curve. Nevertheless, considering the results from bathy Agp2 and canonical DrBphP, whose protein sequences are analog species of PaBphP, it is expected that a secondary structural change from α helix to β sheet around the PHY arm is also involved in the photocycle of PaBphP. Accordingly, it can be inferred that although the light-induced transitions of bathy and canonical BphPs involve similar local structural changes around the chromophore region, their global conformational changes are quite different.

Most full-length BphPs, as summarized in fig. S1C, adopt dimeric modular structures consisting of the typical PAS-GAF-PHY-HK arrangement in which the domains are sequentially linked to their long central helical backbones (*10*, *48*–*50*). This structural characteristic of full-length BphPs regulates the direct interactions between the domains. Nevertheless, it has still been unsolved how the photoinduced structural change in the photosensory module can propagate over a long distance to the output HK domain during signal transduction (*48*). To obtain structural insights into full-length PaBphPs, we performed additional homology modeling with the aid of an MD simulation based on energy minimization by following a well-established approach (*6*, *42*). In this procedure, the HK from *Thermotoga maritima*, composed of the dimerization histidine phosphotransfer domain (DHp) and the catalytic adenosine triphosphate–binding domain (denoted CA), was used as the homologous HK domain for the full-length PaBphP (*51*). This modeled full-length structure of the parental Pfr state of PaBphP shows that the DHp domains use their helical spines to form a spatial gap at their dimeric interface. In the photoproduct Pr state, the helical spines are twisted together, and the degree of the spatial gap between the DHp domains decreases, resulting in a decreased distance between the CA domains when compared to the Pfr state (Fig. 5). In the crystal structure of the Pr state of bathy-like full-length BphP from *Xanthomonas campestris* (XccBphP) (*48*, *49*), quaternary structural assemblies were stabilized by numerous salt bridges and nonbonded contacts, forming a tight dimeric association in the output HK domain (fig. S7). These intermolecular interactions may be key components that facilitate close contact with the

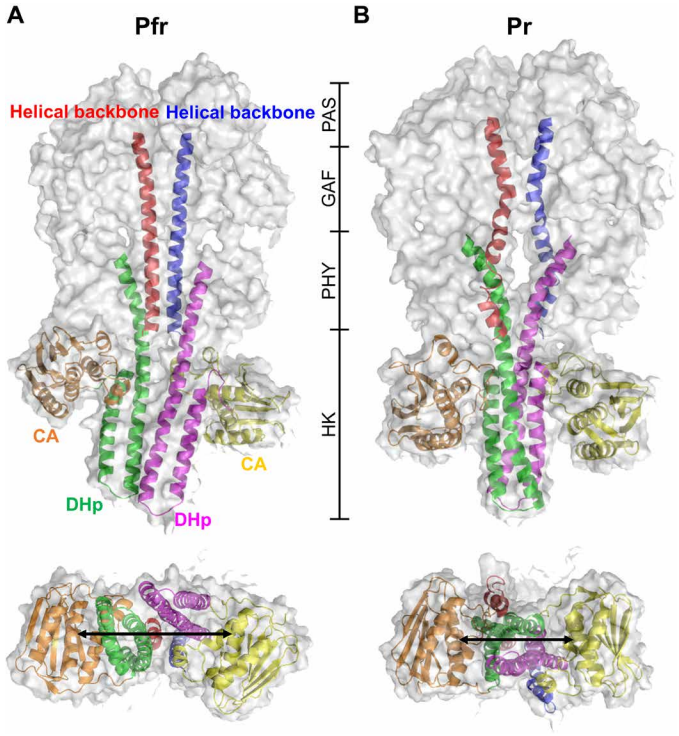

Fig. 5. Reconstructed structures of the full-length PaBphP based on the results from the TRXSS study. (**A**) Reconstructed protein conformation for the Pfr state of full-length PaBphP. (**B**) Reconstructed protein conformation for the Pr state of full-length PaBphP. For clarity, the structures of the CA domains, DHp domains, and helical backbones are represented as cartoon models, and the other structures are represented as translucent surface models. The bottom panels show the bottom view of the full-length constructs, in which the distances between the CA domains are represented by black arrows. The Pr state has a shorter distance between the CA domains than the Pfr state does.

output domain in the Pr state of full-length PaBphP. Therefore, we propose that the light activation of PaBphP induces a large quaternary structural change at the dimeric interface to form the Pr state, where the structural change in the extended central helical bundles causes a change in the quaternary assemblies of the output domain that ultimately regulate biological functions such as phosphorylation. Further studies using authentic full-length constructs are required to experimentally verify the feasibility of the modeled structures of full-length PaBphP reconstructed from protein structures determined using TRXSS.

In this study, we revealed the photoinduced structural dynamics of bathy PaBphP during the light-induced signaling transition from the parental Pfr state to the photoproduct P state, in terms of the global protein structure. The analysis of the TRXSS data leads us to conclude that the far-red light activation of bathy PaBphP involves the structural transitions of the helical backbones from an II-framed close form of Pfr to an O-framed open form of Pr via structurally distinct precursor intermediates (Fig. 4). This conformational change that was observed in bathy PaBphP is significantly different from that in other canonical BphPs. A recent computational study on the Pfr-activated reaction mechanism reported structural changes in the chromophore-binding region (*52*). Despite this trial, information regarding the conformational change and its dynamic behavior in the Pfr-to-Pr transition remains elusive. Our TRXSS study is the

first to visualize the signaling mechanism activated by the parental Pfr state of bathy BphPs in view of the global protein conformation. Although our experimental approach successfully captured the major structural changes associated with the formation of the photoproduct state in PaBphP, further studies with better time resolution and SNR, such as those using serial crystallography (*43*, *53*, *54*), are required to elucidate the local structural changes around the biliverdin chromophore and the PHY arm region, which are presumed to be key structural moieties in the light-induced signaling mechanism. The findings of the current study may contribute to future research to generate more detailed information about BphP structural dynamics.

MATERIALS AND METHODS

Sample preparation

Purified protein samples were prepared according to a previously published protocol (*6*).

Measurement of UV-visible spectra

The ultraviolet (UV)–visible spectra of PaBphP were measured in solution at room temperature from 230 to 900 nm using a Shimadzu UV-1650 spectrometer. The absorption spectra of the Pfr and Pr states were measured in a dark-adapted state and after illumination with fiber optic light at 750 nm (far-red), respectively.

TRXSS experiment

A schematic representation of the TRXSS experiment is shown in Fig. 1B. Polychromatic 12-keV x-ray pulses were generated using a 324-bunch mode operation at the Advanced Photon Source. After irradiation of the protein sample using circularly polarized picosecond laser pulses (pump) with a fluence of 1 mJ/mm^2 at 780 nm, polychromatic x-ray pulses (probe) were delivered to observe the laser-induced structural changes recorded in SAXS/wide-angle x-ray scattering (WAXS) patterns. For each time delay between the pump and probe pulses, a pump-probe measurement was performed at a rate of 10 Hz, with a time spacing of 100 ms between pulses. The x-ray scattering patterns over the wide time range from 10 μs to 10 ms were recorded using a Mar165 charge-coupled device detector (Rayonix, USA). The scattering pattern at a negative time delay (−50 μs) was also collected and used as a reference for calculating the differences in the scattering curves. The scattering pattern at −50-μs time delay contains structural information of the initial state, while the data at positive time delays contains contributions from a mixture of the initial state, intermediates, and photoproducts. The difference scattering curves, $\Delta S(q, t) = S(q, t) - S(q, -50\ \mu s)$, were generated by subtracting the scattering curve at −50 μs from the curves at positive time delays. For each time delay, more than 100 scattering curves were averaged to achieve a high SNR, and measurements were performed at 295 K using a cold nitrogen stream (Oxford Cryostream). A solution of 130 μM (30 mg/ml) photosensory module of PaBphP dissolved in 50 mM tris buffer (pH 8.0) was used for the measurements. The sample solution was passed through a capillary flow cell at a rate of 15 μl/s using a syringe-free pump (Valco Instruments). During the measurement, the sample solution in the reservoir was photosaturated by continuous illumination with red light, which made the ratio of Pfr to Pr constant. To provide red light to the sample reservoir, a wavelength longer than 640 nm was selected by transmitting the lamp light generated from the fiber optic lamp (Fiber-Lite DC950) into a band-pass filter. To check the effect of the illumination on the sample reservoir, we additionally assessed the raw static scattering curves measured at a negative time delay, which were used as the reference signal to generate the difference scattering curve for positive time delays. No significant changes were observed in the shape of the raw static scattering curves with the negative time delay measured in each cycle during the time-resolved measurements. From this, it could be conjectured that the population ratio between the Pfr and Pr states of the sample subjected to the pump and probe measurements was well maintained during the data collection.

Global kinetic analysis for TRXSS data

Before the global kinetic analysis, the datasets for time series 1 (10 μs to 3.16 ms) and time series 2 (100 μs to 10 ms) were merged to produce the combined experimental data that ranged from 10 μs to 10 ms. The global kinetic analysis for each dataset confirmed that merging the two datasets would not cause any data distortion (see the Supplementary Materials and figs. S2 and S4). The curves from time series 1 were scaled so that the scattering intensities of the curves from two different time series matched each other at common time delays from 100 μs to 3.16 ms (fig. S2A). Subsequently, the sets of curves from time series 1 and 2 were combined by averaging the curves of the two different time series at each common time delay, and a set of combined experimental scattering curves with time delays from 10 μs to 10 ms were obtained. The difference scattering signal caused by laser-induced solvent heating, which affects the scattering signals in the wide-angle region (see the Supplementary Materials for details), was removed using a well-established protocol (*55*–*57*).

To determine the kinetics of the structural transitions in PaBphP, SVD was applied to the set of solvent heating-free experimental scattering curves (TRXSS data) (*55*–*58*). SVD analysis decomposes the data matrix of time-resolved difference scattering curves, A, into three matrices U, S, and V satisfying the relationship of $A = USV^{T}$, where U is a matrix of columns called left singular vectors (LSVs), composed of time-independent q spectra, V is a matrix of columns called RSVs, composed of time-dependent amplitude changes to the LSVs, and S is a matrix whose diagonal elements are the weights of the singular vectors. LSVs provide a basis of the space spanned by SADSs, while RSVs represent the population dynamics of these transient intermediates. Thus, SVD analysis allows us to obtain the number of structurally distinct species and the dynamics of each species, regardless of the kinetic model. From the SVD analysis in the time range from 10 μs to 10 ms, we identified three significant singular vectors determined on the basis of the singular values and autocorrelation factors of the corresponding singular vectors (fig. S2, B and C). We note that the spectral feature of LSV3 (the third LSV) is marginal when compared with the first two LSVs, but the feature of RSV3 (the third RSV) seems to be meaningful in terms of the temporal profile. Therefore, we included the first three singular vectors to account for the entire kinetics in the measured time series, as shown in fig. S4. By globally fitting the first three RSVs using exponentials sharing two common relaxation times, time constants of 95 (± 25) μs and 21 (± 32) ms were obtained. Using the kinetic components for the transitions from first species to third species obtained from the SVD analysis, we applied PCA to decompose the experimental scattering curves into three SADSs corresponding to the three species as follows

$$\Delta S_{\text{theory}}(q_i, t_j) = \sum_{k=1}^{3} [\, C_k(t_j)\,] \Delta S_{C_k}(q_i) \quad (1)$$

where $\Delta S_{theory}(q_i, t_j)$ is the theoretical difference scattering curve at given q and t values, $\Delta S_{Ck}(q_i)$ is the SADS corresponding to the kth intermediate species at a given q value, and $C_k(t_j)$ is the instantaneous population of the kth intermediate at a given t value and can be calculated using the time constants obtained from the SVD analysis. We then applied the Nelder-Mead simplex algorithm to minimize the discrepancy between the theoretical and experimental curves.

MD simulations to generate candidate structures for the analysis of TRXSS data

We used structural analysis aided by MD simulations to extract three-dimensional protein conformations from the two SADSs (SADS2 and SADS3) obtained from the experimental curves. Representative protein structures were simulated as follows: structures with a (i) II-framed, (ii) O-framed, and (iii) Y-framed geometry in terms of their helical backbones.

First, we performed the MD simulation using an x-ray crystallographic structure with the Protein Data Bank (PDB) entry of 3NHQ (*21*) as the starting structure to generate the equilibrium structures with (i) II-framed geometry in terms of the helical backbones. To do so, the GROMACS 2019.2 package with the Charmm36 force field (*59*) was used, in combination with the SPCE water model. The system was equilibrated under NVT conditions for 100 ps with a velocity-rescale thermostat (τ_T = 0.1 ps, T = 300 K) and was then subsequently equilibrated under NPT conditions for 500 ps with a velocity-rescale thermostat (τ_T = 0.1 ps, T = 300 K) and a Parrinello-Rahman barostat (τ_T = 0.5 ps, P = 1 bar). A 10-ns-long production simulation was then conducted using the equilibrated structure. After the simulation, the candidate structures for (i) were sampled at 100-ps intervals from the MD trajectory. From the structures in the MD trajectory, the representative structure was also selected by using the clustering method. Using the representative structure with the II-framed geometry as a starting structure, we then performed NEMD simulations to generate plausible protein conformations for (ii) an O-framed geometry and (iii) a Y-framed geometry using the pulling algorithm in GROMACS.

To generate (ii) structures with an O-framed geometry in terms of the helical backbones, we set two residues, Arg^{321} and Ala^{332}, on each helical backbone as positions where the external pulling force would be applied. In the pulling simulation, the same pulling force strength of 1000 kJ/mol/nm^2 was applied at both positions. The maximum distance between Arg^{321} residues (Q1) in the pulling simulation was allowed to be much longer than that between the Ala^{332} residues (Q2), which facilitated the generation of O-framed geometry, as shown in fig. S1C. Considering the conformational diversity of the structure pool with an O-framed geometry, we repeated six different pulling simulations with different maximum values of Q2 (fig. S5, A to F). For each simulation, Q1 was allowed to increase to ~7.0 nm, and Q2 was allowed to increase to a value between ~3.0 and ~7.0 nm. All NEMD simulations were performed using the pulling algorithm along the hypothetical reaction coordinates until the value of Q1 reached ~7 nm. In the crystal structure of the Pr state for DrBphP (*8*, *23*), the distance between the separated linker helices, corresponding to Q1 in PaBphP, was ~4.07 nm. On the basis of this distance in DrBphP, among the MD-generated structures, we sampled the candidate structures with a Q1 ranging from 3 to 5 nm. A total of 1500 structures with O-framed geometries were selected from six different NEMD trajectories. To generate (iii) structures with a Y-framed geometry, we identified the center of mass (COM) of the residues from Ser^{291} to Asp^{333}, on each helical backbone. During the NEMD simulation using the pulling algorithm, a constant pulling force of 1000 kJ/mol/nm^2 was applied to the two COMs, and the distance between them was gradually increased to form a Y-framed geometry (fig. S5G). The NEMD simulation was implemented until the COM-COM distance reached ~8 nm (fig. S5G). A total of 200 structures with a Y-framed geometry were evenly sampled from the NEMD trajectory.

Meanwhile, during the NEMD simulations, helical distortions were observed in the vicinity of Arg^{321} residues. To investigate the effects of helical distortions on the structural analysis, we chose MD-generated structures with and without helical distortions. From these structures, the theoretical difference curves were calculated using the same Pfr structure as a reference structure, and each curve was compared with the experimental curve. The details of the helical distortion effects in the theoretical scattering curves are described in the Supplementary Materials and fig. S8.

Refinement of MD-generated structures to obtain optimal structures

Using the MD-generated structures, the protein conformations that well describe the SADSs were obtained by comparing the experimental scattering curves and theoretical scattering curves from the simulated structures. The theoretical scattering curves for the MD-generated structures were calculated using the CRYSOL program (*60*), and the theoretical "difference scattering curves" were generated by subtracting the theoretical static scattering curves for Pfr from those for I_2 (or P). Details of the calculations performed by CRYSOL are described in the Supplementary Materials and fig. S9. We also convoluted the energy spectrum of the x-ray pulse with the theoretical scattering signal to consider the effect of the polychromatic x-ray beam by following well-established protocols (*57*). After generating the pools of the theoretical difference scattering curves, the theoretical difference x-ray scattering curves were compared with two SADSs to find the optimal structures of I_2 and P. In this procedure, we calculated the reduced χ^2_{red} value, which is an indicator of the discrepancy between the theoretical difference scattering curve and the experimental data as follows

$$\chi^2_{red} = \frac{1}{N-1}\sum_{i=1}^{N}\left[\frac{\mu \cdot \Delta S_{theory}(q_i) - \Delta S_{exp}(q_i)}{\sigma(q_i)}\right]^2 \quad (2)$$

where $\Delta S_{theory}(q)$ is the theoretical difference in the x-ray scattering curve, $\Delta S_{exp}(q)$ is the experimental TRXSS data, μ is the scaling factor between $\Delta S_{theory}(q)$ and $\Delta S_{exp}(q)$, N is the number of experimental q points, and $\sigma(q)$ is the experimental SD. The scaling factor (μ) consists of two parameters: (i) the relative ratio between the experimental and theoretical scattering curves and (ii) the effective photoreaction yield of PaBphP. Details regarding the effective photoreaction yield are provided in the Supplementary Materials. In principle, a χ^2_{red} value close to 1 represents the most optimal solution within the experimental error. As the scattering feature of SADS1 is insignificant within the experimental resolution, we performed structural refinement of SADS2 and SADS3. In the structural analysis, we assumed that the Pfr, I_2, and P states could adopt one of the three frames (II-frame, O-frame, and Y-frame) in terms of helical backbones. Considering the assumption that both Pfr and I_2 (or P) have three possibilities (II-frame, O-frame, and Y-frame), nine combinations

are possible, as summarized in Fig. 3. On the basis of all possible combinations, the theoretical difference curves with the lowest χ^2_{red} values for SADS2 and SADS3 were selected as the optimal solutions, and the optimal protein structures of I_2 and P were obtained from the MD-generated structures used to generate these theoretical difference curves.

After the structural analysis, we analyzed the static scattering curve for the dark-adapted PaBphP using the structures of dimers and monomers for the Pfr and Pr states obtained from the structural analysis (Fig. 3, C and F). The structures of the monomers were reconstructed from half that of the dimers. The theoretical scattering curves were calculated from the dimer and reconstructed monomer structures and were used to describe the experimental curve. The relative fractions of monomers, dimer Pfr, and dimer Pr were fitted until the theoretical scattering curve showed good agreement with the experimental curve. The details and further discussion of this analysis are provided in the Supplementary Materials and fig. S10 (A and B).

In addition, to investigate the effects of the monomer-related transitions on the difference scattering curve, we performed an additional structural analysis on the basis of the modeled structures of the dimeric and monomeric forms. The theoretical difference scattering curves corresponding to the monomer-related transitions were compared with the experimental data (SADS2 and SADS3). The difference scattering curves for the dimer-to-dimer transition are in good agreement with the experimental data, whereas those for the monomer-related transitions fail to describe the experimental data (fig. S10, C and D). The details and further discussion of this analysis are provided in the Supplementary Materials and fig. S10 (C and D).

Modeling the full-length PaBphP construct

Full-length PaBphP constructs of Pfr and Pr were modeled by combining the structures of the photosensory modules of PaBPhP determined in this study, based on the TRXSS data and homology information of the output domain. The Pfr and Pr structures from the structural analysis of the TRXSS data were used as the photosensory modules, and the output domain was adopted from the HK moiety of *T. maritima*, as reported in a crystallographic study (PDB ID: 2C2A) (*10*, *48*–*50*). To model the full-length Pfr construct, the HK domain moiety was connected to the C terminus of the Pfr structure of the photosensory modules. Using this structure as a starting point, MD simulations were conducted to obtain the equilibrated conformation in the solution phase. The full-length construct was solvated in a periodic cubic box with explicit water molecules, which was neutralized by sodium ions. The system was equilibrated under NVT conditions for 100 ps with a velocity-rescale thermostat (τ_T = 0.1 ps, T = 300 K) and subsequently equilibrated under NPT conditions for 500 ps with a velocity-rescale thermostat (τ_T = 0.1 ps, T = 300 K) and a Parrinello-Rahman barostat (τ_T = 0.5 ps, P = 1 bar). After equilibration, production simulation was conducted using the equilibrated structure for 100 ns. To model the full-length construct of Pr, the HK domain moiety was connected to the C terminus of the Pr structure of the photosensory modules, and the same procedure used in the modeling of the full-length construct for Pfr was applied to this structure.

SUPPLEMENTARY MATERIALS

Supplementary material for this article is available at https://science.org/doi/10.1126/sciadv.abm6278

View/request a protocol for this paper from *Bio-protocol*.

REFERENCES AND NOTES

1. E. Giraud, S. Zappa, L. Vuillet, J. M. Adriano, L. Hannibal, J. Fardoux, C. Berthomieu, P. Bouyer, D. Pignol, A. Verméglio, A new type of bacteriophytochrome acts in tandem with a classical bacteriophytochrome to control the antennae synthesis in Rhodopseudomonas palustris. *J. Biol. Chem.* **280**, 32389–32397 (2005).
2. M. Gomelsky, W. D. Hoff, Light helps bacteria make important lifestyle decisions. *Trends Microbiol.* **19**, 441–448 (2011).
3. T. Lamparter, P. Xue, A. Elkurdi, G. Kaeser, L. Sauthof, P. Scheerer, N. Krauß, Phytochromes in *Agrobacterium fabrum*. *Front. Plant Sci.* **12**, 642801 (2021).
4. N. C. Rockwell, Y. S. Su, J. C. Lagarias, Phytochrome structure and signaling mechanisms. *Annu. Rev. Plant Biol.* **57**, 837–858 (2006).
5. P. Scheerer, N. Michael, J. H. Park, S. Nagano, H. W. Choe, K. Inomata, B. Borucki, N. Krauss, T. Lamparter, Light-induced conformational changes of the chromophore and the protein in phytochromes: Bacterial phytochromes as model systems. *ChemPhysChem* **11**, 1090–1105 (2010).
6. X. Yang, J. Kuk, K. Moffat, Crystal structure of *Pseudomonas aeruginosa* bacteriophytochrome: Photoconversion and signal transduction. *Proc. Natl. Acad. Sci. U.S.A.* **105**, 14715–14720 (2008).
7. X. Yang, J. Kuk, K. Moffat, Conformational differences between the Pfr and Pr states in *Pseudomonas aeruginosa* bacteriophytochrome. *Proc. Natl. Acad. Sci. U.S.A.* **106**, 15639–15644 (2009).
8. H. Takala, A. Björling, O. Berntsson, H. Lehtivuori, S. Niebling, M. Hoernke, I. Kosheleva, R. Henning, A. Menzel, J. A. Ihalainen, S. Westenhoff, Signal amplification and transduction in phytochrome photosensors. *Nature* **509**, 245–248 (2014).
9. X. Yang, E. A. Stojković, W. B. Ozarowski, J. Kuk, E. Davydova, K. Moffat, Light signaling mechanism of two tandem bacteriophytochromes. *Structure* **23**, 1179–1189 (2015).
10. D. Bellini, M. Z. Papiz, Structure of a bacteriophytochrome and light-stimulated protomer swapping with a gene repressor. *Structure* **20**, 1436–1446 (2012).
11. L. O. Essen, J. Mailliet, J. Hughes, The structure of a complete phytochrome sensory module in the Pr ground state. *Proc. Natl. Acad. Sci. U.S.A.* **105**, 14709–14714 (2008).
12. J. Mailliet, G. Psakis, K. Feilke, V. Sineshchekov, L. O. Essen, J. Hughes, Spectroscopy and a high-resolution crystal structure of Tyr263 mutants of cyanobacterial phytochrome Cph1. *J. Mol. Biol.* **413**, 115–127 (2011).
13. N. C. Rockwell, S. S. Martin, J. C. Lagarias, Red/green cyanobacteriochromes: Sensors of color and power. *Biochemistry* **51**, 9667–9677 (2012).
14. D. Wang, Y. Qin, S. Zhang, L. Wang, X. Yang, D. Zhong, Elucidating the molecular mechanism of ultrafast Pfr-state photoisomerization in bathy bacteriophytochrome PaBphP. *J. Phys. Chem. Lett.* **10**, 6197–6201 (2019).
15. D. Wang, Y. Qin, M. Zhang, X. Li, L. Wang, X. Yang, D. Zhong, The origin of ultrafast multiphasic dynamics in photoisomerization of bacteriophytochrome. *J. Phys. Chem. Lett.* **11**, 5913–5919 (2020).
16. J. J. van Thor, M. Mackeen, I. Kuprov, R. A. Dwek, M. R. Wormald, Chromophore structure in the photocycle of the cyanobacterial phytochrome Cph1. *Biophys. J.* **91**, 1811–1822 (2006).
17. R. Tasler, T. Moises, N. Frankenberg-Dinkel, Biochemical and spectroscopic characterization of the bacterial phytochrome of *Pseudomonas aeruginosa*. *FEBS J.* **272**, 1927–1936 (2005).
18. B. Karniol, R. D. Vierstra, The pair of bacteriophytochromes from *Agrobacterium tumefaciens* are histidine kinases with opposing photobiological properties. *Proc. Natl. Acad. Sci. U.S.A.* **100**, 2807–2812 (2003).
19. S. R. Tachibana, L. Tang, C. Chen, L. Zhu, Y. Takeda, K. Fushimi, T. K. Seevers, R. Narikawa, M. Sato, C. Fang, Transient electronic and vibrational signatures during reversible photoswitching of a cyanobacteriochrome photoreceptor. *Spectrochim. Acta A Mol. Biomol. Spectrosc.* **250**, 119379 (2021).
20. A. E. Fitzpatrick, C. N. Lincoln, L. J. G. W. van Wilderen, J. J. van Thor, Pump–dump–probe and pump–repump–probe ultrafast spectroscopy resolves cross section of an early ground state intermediate and stimulated emission in the photoreactions of the Pr ground state of the cyanobacterial phytochrome Cph1. *J. Phys. Chem. B* **116**, 1077–1088 (2012).
21. X. Yang, Z. Ren, J. Kuk, K. Moffat, Temperature-scan cryocrystallography reveals reaction intermediates in bacteriophytochrome. *Nature* **479**, 428–432 (2011).
22. A. Schmidt, L. Sauthof, M. Szczepek, M. F. Lopez, F. V. Escobar, B. M. Qureshi, N. Michael, D. Buhrke, T. Stevens, D. Kwiatkowski, D. von Stetten, M. A. Mroginski, N. Krauß, T. Lamparter, P. Hildebrandt, P. Scheerer, Structural snapshot of a bacterial phytochrome in its functional intermediate state. *Nat. Commun.* **9**, 4912 (2018).
23. E. S. Burgie, J. Zhang, R. D. Vierstra, Crystal structure of deinococcus phytochrome in the photoactivated state reveals a cascade of structural rearrangements during photoconversion. *Structure* **24**, 448–457 (2016).
24. R. Neutze, R. Wouts, S. Techert, J. Davidsson, M. Kocsis, A. Kirrander, F. Schotte, M. Wulff, Visualizing photochemical dynamics in solution through picosecond x-ray scattering. *Phys. Rev. Lett.* **87**, 195508 (2001).

25. H. Ihee, M. Lorenc, T. K. Kim, Q. Y. Kong, M. Cammarata, J. H. Lee, S. Bratos, M. Wulff, Ultrafast x-ray diffraction of transient molecular structures in solution. *Science* **309**, 1223–1227 (2005).
26. M. Cammarata, M. Levantino, F. Schotte, P. A. Anfinrud, F. Ewald, J. Choi, A. Cupane, M. Wulff, H. Ihee, Tracking the structural dynamics of proteins in solution using time-resolved wide-angle x-ray scattering. *Nat. Methods* **5**, 881–886 (2008).
27. H. Ihee, Visualizing solution-phase reaction dynamics with time-resolved x-ray liquidography. *Acc. Chem. Res.* **42**, 356–366 (2009).
28. H. S. Cho, N. Dashdorj, F. Schotte, T. Graber, R. Henning, P. Anfinrud, Protein structural dynamics in solution unveiled via 100-ps time-resolved x-ray scattering. *Proc. Natl. Acad. Sci. U.S.A.* **107**, 7281–7286 (2010).
29. D. Arnlund, L. C. Johansson, C. Wickstrand, A. Barty, G. J. Williams, E. Malmerberg, J. Davidsson, D. Milathianaki, D. P. DePonte, R. L. Shoeman, D. Wang, D. James, G. Katona, S. Westenhoff, T. A. White, A. Aquila, S. Bari, P. Berntsen, M. Bogan, T. B. van Driel, R. B. Doak, K. S. Kjær, M. Frank, R. Fromme, I. Grotjohann, R. Henning, M. S. Hunter, R. A. Kirian, I. Kosheleva, C. Kupitz, M. Liang, A. V. Martin, M. M. Nielsen, M. Messerschmidt, M. M. Seibert, J. Sjöhamn, F. Stellato, U. Weierstall, N. A. Zatsepin, J. C. H. Spence, P. Fromme, I. Schlichting, S. Boutet, G. Groenhof, H. N. Chapman, R. Neutze, Visualizing a protein quake with time-resolved x-ray scattering at a free-electron laser. *Nat. Methods* **11**, 923–926 (2014).
30. J. G. Kim, T. W. Kim, J. Kim, H. Ihee, Protein structural dynamics revealed by time-resolved x-ray solution scattering. *Acc. Chem. Res.* **48**, 2200–2208 (2015).
31. T. B. van Driel, K. S. Kjær, R. W. Hartsock, A. O. Dohn, T. Harlang, M. Chollet, M. Christensen, W. Gawelda, N. E. Henriksen, J. G. Kim, K. Haldrup, K. H. Kim, H. Ihee, J. Kim, H. Lemke, Z. Sun, V. Sundström, W. Zhang, D. Zhu, K. B. Møller, M. M. Nielsen, K. J. Gaffney, Atomistic characterization of the active-site solvation dynamics of a model photocatalyst. *Nat. Commun.* **7**, 13678 (2016).
32. D. Rimmerman, D. Leshchev, D. J. Hsu, J. Hong, I. Kosheleva, L. X. Chen, Direct observation of insulin association dynamics with time-resolved x-ray scattering. *J. Phys. Chem. Lett.* **8**, 4413–4418 (2017).
33. K. Haldrup, G. Levi, E. Biasin, P. Vester, M. G. Laursen, F. Beyer, K. S. Kjær, T. Brandt van Driel, T. Harlang, A. O. Dohn, R. J. Hartsock, S. Nelson, J. M. Glownia, H. T. Lemke, M. Christensen, K. J. Gaffney, N. E. Henriksen, K. B. Møller, M. M. Nielsen, Ultrafast x-ray scattering measurements of coherent structural dynamics on the ground-state potential energy surface of a diplatinum molecule. *Phys. Rev. Lett.* **122**, 063001 (2019).
34. D. J. Hsu, D. Leshchev, D. Rimmerman, J. Hong, M. S. Kelley, I. Kosheleva, X. Zhang, L. X. Chen, X-ray snapshots reveal conformational influence on active site ligation during metalloprotein folding. *Chem. Sci.* **10**, 9788–9800 (2019).
35. K. Kunnus, M. Vacher, T. C. B. Harlang, K. S. Kjær, K. Haldrup, E. Biasin, T. B. van Driel, M. Pápai, P. Chabera, Y. Liu, H. Tatsuno, C. Timm, E. Källman, M. Delcey, R. W. Hartsock, M. E. Reinhard, S. Koroidov, M. G. Laursen, F. B. Hansen, P. Vester, M. Christensen, L. Sandberg, Z. Németh, D. S. Szemes, É. Bajnóczi, R. Alonso-Mori, J. M. Glownia, S. Nelson, M. Sikorski, D. Sokaras, H. T. Lemke, S. E. Canton, K. B. Møller, M. M. Nielsen, G. Vankó, K. Wärnmark, V. Sundström, P. Persson, M. Lundberg, J. Uhlig, K. J. Gaffney, Vibrational wavepacket dynamics in Fe carbene photosensitizer determined with femtosecond x-ray emission and scattering. *Nat. Commun.* **11**, 634 (2020).
36. H. Ravishankar, M. N. Pedersen, M. Eklund, A. Sitsel, C. Li, A. Duelli, M. Levantino, M. Wulff, A. Barth, C. Olesen, P. Nissen, M. Andersson, Tracking Ca^{2+} ATPase intermediates in real time by x-ray solution scattering. *Sci. Adv.* **6**, eaaz0981 (2020).
37. K. S. Kjær, T. B. Van Driel, T. C. B. Harlang, K. Kunnus, E. Biasin, K. Ledbetter, R. W. Hartsock, M. E. Reinhard, S. Koroidov, L. Li, M. G. Laursen, F. B. Hansen, P. Vester, M. Christensen, K. Haldrup, M. M. Nielsen, A. O. Dohn, M. I. Pápai, K. B. Møller, P. Chabera, Y. Liu, H. Tatsuno, C. Timm, M. Jarenmark, J. Uhlig, V. Sundström, K. Wärnmark, P. Persson, Z. Németh, D. S. Szemes, É. Bajnóczi, G. Vankó, R. Alonso-Mori, J. M. Glownia, S. Nelson, M. Sikorski, D. Sokaras, S. E. Canton, H. T. Lemke, K. J. Gaffney, Finding intersections between electronic excited state potential energy surfaces with simultaneous ultrafast x-ray scattering and spectroscopy. *Chem. Sci.* **10**, 5749–5760 (2019).
38. S. J. Lee, Y. Kim, T. W. Kim, C. Yang, K. Thamilselvan, H. Jeong, J. Hyun, H. Ihee, Reversible molecular motional switch based on circular photoactive protein oligomers exhibits unexpected photo-induced contraction. *Cell Rep. Phys. Sci.* **2**, 100512 (2021).
39. Y. Lee, J. G. Kim, S. J. Lee, S. Muniyappan, T. W. Kim, H. Ki, H. Kim, J. Jo, S. R. Yun, H. Lee, K. W. Lee, S. O. Kim, M. Cammarata, H. Ihee, Ultrafast coherent motion and helix rearrangement of homodimeric hemoglobin visualized with femtosecond x-ray solution scattering. *Nat. Commun.* **12**, 3677 (2021).
40. V. Zoete, M. A. Cuendet, A. Grosdidier, O. Michielin, SwissParam: A fast force field generation tool for small organic molecules. *J. Comput. Chem.* **32**, 2359–2368 (2011).
41. M. J. Abraham, T. Murtola, R. Schulz, S. Páll, J. C. Smith, B. Hess, E. Lindahl, GROMACS: High performance molecular simulations through multi-level parallelism from laptops to supercomputers. *Softwarex* **1-2**, 19–25 (2015).
42. A. Björling, O. Berntsson, H. Lehtivuori, H. Takala, A. J. Hughes, M. Panman, M. Hoernke, S. Niebling, L. Henry, R. Henning, I. Kosheleva, V. Chukharev, N. V. Tkachenko, A. Menzel, G. Newby, D. Khakhulin, M. Wulff, J. A. Ihalainen, S. Westenhoff, Structural photoactivation of a full-length bacterial phytochrome. *Sci. Adv.* **2**, e1600920 (2016).
43. E. Claesson, W. Y. Wahlgren, H. Takala, S. Pandey, L. Castillon, V. Kuznetsova, L. Henry, M. Panman, M. Carrillo, J. Kübel, R. Nanekar, L. Isaksson, A. Nimmrich, A. Cellini, D. Morozov, M. Maj, M. Kurttila, R. Bosman, E. Nango, R. Tanaka, T. Tanaka, L. Fangjia, S. Iwata, S. Owada, K. Moffat, G. Groenhof, E. A. Stojković, J. A. Ihalainen, M. Schmidt, S. Westenhoff, The primary structural photoresponse of phytochrome proteins captured by a femtosecond x-ray laser. *eLife* **9**, e53514 (2020).
44. E. Consiglieri, A. Gutt, W. Gärtner, L. Schubert, C. Viappiani, S. Abbruzzetti, A. Losi, Dynamics and efficiency of photoswitching in biliverdin-binding phytochromes. *Photochem. Photobiol. Sci.* **18**, 2484–2496 (2019).
45. D. J. Heyes, S. J. O. Hardman, M. N. Pedersen, J. Woodhouse, E. De La Mora, M. Wulff, M. Weik, M. Cammarata, N. S. Scrutton, G. Schirò, Light-induced structural changes in a full-length cyanobacterial phytochrome probed by time-resolved x-ray scattering. *Commun. Biol.* **2**, 1 (2019).
46. L. Isaksson, E. Gustavsson, C. Persson, U. Brath, L. Vrhovac, G. Karlsson, V. Orekhov, S. Westenhoff, Signaling mechanism of phytochromes in solution. *Structure* **29**, 151–160.e3 (2021).
47. X. Yang, E. A. Stojkovic, J. Kuk, K. Moffat, Crystal structure of the chromophore binding domain of an unusual bacteriophytochrome, RpBphP3, reveals residues that modulate photoconversion. *Proc. Natl. Acad. Sci. U.S.A.* **104**, 12571–12576 (2007).
48. L. H. Otero, S. Klinke, J. Rinaldi, F. Velázquez-Escobar, M. A. Mroginski, M. Fernández López, F. Malamud, A. A. Vojnov, P. Hildebrandt, F. A. Goldbaum, H. R. Bonomi, Structure of the full-length bacteriophytochrome from the plant pathogen *Xanthomonas campestris* provides clues to its long-range signaling mechanism. *J. Mol. Biol.* **428**, 3702–3720 (2016).
49. V. Conforte, L. H. Otero, L. Toum, S. Sirigu, G. T. Antelo, J. Rinaldi, S. Foscaldi, S. Klinke, L. M. G. Chavas, A. A. Vojnov, F. A. Goldbaum, F. Malamud, H. R. Bonomi, Pr-favoured variants of the bacteriophytochrome from the plant pathogen *Xanthomonas campestris* hint on light regulation of virulence-associated mechanisms. *FEBS. J.* **288**, 5986–6002 (2021).
50. G. Gourinchas, S. Etzl, C. Göbl, U. Vide, T. Madl, A. Winkler, Long-range allosteric signaling in red light-regulated diguanylyl cyclases. *Sci. Adv.* **3**, e1602498 (2017).
51. A. Marina, C. D. Waldburger, W. A. Hendrickson, Structure of the entire cytoplasmic portion of a sensor histidine-kinase protein. *EMBO J.* **24**, 4247–4259 (2005).
52. V. Macaluso, G. Salvadori, L. Cupellini, B. Mennucci, The structural changes in the signaling mechanism of bacteriophytochromes in solution revealed by a multiscale computational investigation. *Chem. Sci.* **12**, 5555–5565 (2021).
53. J. G. Kim, S. Nozawa, H. Kim, E. H. Choi, T. Sato, T. W. Kim, K. H. Kim, H. Ki, J. Kim, M. Choi, Y. Lee, J. Heo, K. Y. Oang, K. Ichiyanagi, R. Fukaya, J. H. Lee, J. Park, I. Eom, S. H. Chun, S. Kim, M. Kim, T. Katayama, T. Togashi, S. Owada, M. Yabashi, S. J. Lee, S. Lee, C. W. Ahn, D.-S. Ahn, J. Moon, S. Choi, J. Kim, T. Joo, J. Kim, S.-i. Adachi, H. Ihee, Mapping the emergence of molecular vibrations mediating bond formation. *Nature* **582**, 520–524 (2020).
54. G. D. Calvey, A. M. Katz, K. A. Zielinski, B. Dzikovski, L. Pollack, Characterizing enzyme reactions in microcrystals for effective mix-and-inject experiments using x-ray free-electron lasers. *Anal. Chem.* **92**, 13864–13870 (2020).
55. K. H. Kim, J. G. Kim, S. Nozawa, T. Sato, K. Y. Oang, T. W. Kim, H. Ki, J. Jo, S. Park, C. Song, T. Sato, K. Ogawa, T. Togashi, K. Tono, M. Yabashi, T. Ishikawa, J. Kim, R. Ryoo, J. Kim, H. Ihee, S.-i. Adachi, Direct observation of bond formation in solution with femtosecond x-ray scattering. *Nature* **518**, 385–389 (2015).
56. T. W. Kim, C. Yang, Y. Kim, J. G. Kim, J. Kim, Y. O. Jung, S. Jun, S. J. Lee, S. Park, I. Kosheleva, R. Henning, J. J. van Thor, H. Ihee, Combined probes of x-ray scattering and optical spectroscopy reveal how global conformational change is temporally and spatially linked to local structural perturbation in photoactive yellow protein. *Phys. Chem. Chem. Phys.* **18**, 8911–8919 (2016).
57. T. W. Kim, S. J. Lee, J. Jo, J. G. Kim, H. Ki, C. W. Kim, K. H. Cho, J. Choi, J. H. Lee, M. Wulff, Y. M. Rhee, H. Ihee, Protein folding from heterogeneous unfolded state revealed by time-resolved x-ray solution scattering. *Proc. Natl. Acad. Sci. U.S.A.* **117**, 14996–15005 (2020).
58. K. H. Kim, S. Muniyappan, K. Y. Oang, J. G. Kim, S. Nozawa, T. Sato, S.-y. Koshihara, R. Henning, I. Kosheleva, H. Ki, Y. Kim, T. W. Kim, J. Kim, S.-I. Adachi, H. Ihee, Direct observation of cooperative protein structural dynamics of homodimeric hemoglobin from 100 ps to 10 ms with pump–probe x-ray solution scattering. *J. Am. Chem. Soc.* **134**, 7001–7008 (2012).
59. J. Huang, S. Rauscher, G. Nawrocki, T. Ran, M. Feig, B. L. de Groot, H. Grubmüller, A. D. MacKerell, CHARMM36m: An improved force field for folded and intrinsically disordered proteins. *Nat. Methods* **14**, 71–73 (2017).
60. D. Svergun, C. Barberato, M. H. Koch, CRYSOL–A program to evaluate x-ray solution scattering of biological macromolecules from atomic coordinates. *J. Appl. Cryst.* **28**, 768–773 (1995).

Acknowledgments: We acknowledge extensive support from I. Kosheleva and R. Henning of the ID14B beamline at Advanced Photon Source during data collection there. **Funding:** Use of the BioCARS Sector 14 was also supported by the National Institutes of Health, National Institute of General Medical Sciences grant R24GM111072. The time-resolved setup at Sector 14 was funded in part through collaboration with P. Anfinrud (NIH/NIDDK) through the Intramural Research Program of the NIDDK. Use of the Advanced Photon Source was supported by the U.S. Department of Energy, Basic Energy Sciences, Office of Science, under contract no. DE-AC02-06CH11357. This work was supported by the Institute for Basic Science (IBS-R033). This work was supported by National Institutes of Health grants GM036452 to K.M. and EY024363 to X.Y. **Author contributions:** T.W.K., X.Y., and H.I. designed research; J.K. and I.K. prepared protein sample; Z.R. and X.Y. performed static experiments; T.W.K., J.G.K., C.Y., Z.R., X.Y., and H.I. performed TRXSS experiments; S.J.L., T.W.K., Z.R., X.Y., and H.I. analyzed data; S.J.L., T.W.K., K.M., X.Y., and H.I. wrote the paper; and all authors discussed the experimental results. **Competing interests:** The authors declare that they have no competing interests. **Data and materials availability:** All data needed to evaluate the conclusions in the paper are present in the paper and/or the Supplementary Materials.

Submitted 5 October 2021
Accepted 13 April 2022
Published 27 May 2022
10.1126/sciadv.abm6278

ScienceAdvances

Light-induced protein structural dynamics in bacteriophytochrome revealed by time-resolved x-ray solution scattering

Sang Jin LeeTae Wu KimJong Goo KimCheolhee YangSo Ri YunChangin KimZhong RenIndika KumarapperumaJane KukKeith MoffatXiaojing YangHyotcherl Ihee

Sci. Adv., 8 (21), eabm6278. • DOI: 10.1126/sciadv.abm6278

Science Advances (ISSN) is published by the American Association for the Advancement of Science. 1200 New York Avenue NW, Washington, DC 20005. The title *Science Advances* is a registered trademark of AAAS.